Atmospheric Aerosol Outbreak over Nicosia, Cyprus, in April 2019: Case Study

Yuliia Yukhymchuk, Gennadi Milinevsky, Ivan Syniavskyi, Ioana-Elisabeta Popovici, Florin Unga, Jean Sciare, Franco Marenco, Michael Pikridas, Philippe Goloub

atmosphere

MDPI

Article

Atmospheric Aerosol Outbreak over Nicosia, Cyprus, in April 2019: Case Study

Yuliia Yukhymchuk [1,2], Gennadi Milinevsky [1,3,4,*], Ivan Syniavskyi [1], Ioana Popovici [2,5], Florin Unga [6,7], Jean Sciare [6], Franco Marenco [6,8], Michael Pikridas [6] and Philippe Goloub [2]

1 Department for Atmospheric Optics and Instrumentation, Main Astronomical Observatory, 03143 Kyiv, Ukraine
2 Laboratoire d'Optique Atmosphérique, Centre National de la Recherche Scientifique (CNRS), University of Lille, 59000 Lille, France
3 International Center of Future Science, College of Physics, Jilin University, Changchun 130012, China
4 Physics Faculty, Taras Shevchenko National University of Kyiv, 01601 Kyiv, Ukraine
5 Research & Development Department, Cimel Electronique, 75011 Paris, France
6 Climate and Atmosphere Research Centre (CARE-C), The Cyprus Institute, Nicosia 2121, Cyprus
7 National Research Council of Italy, Institute of Atmospheric Sciences and Climate (CNR-ISAC), 73100 Lecce, Italy
8 Space Applications and Nowcasting (SAN), Met Office, Exeter EX1 3PB, UK
* Correspondence: gennadi.milinevsky@knu.ua; Tel.: +380-67-209-6256

Abstract: This paper aims to analyze the significant changes in atmospheric aerosol characteristics during the extreme aerosol outbreak event in April 2019 in the atmosphere over Cyprus in the Eastern Mediterranean. We study the aerosol optical depth (AOD), Ångström exponent (AE), single-scattering albedo, refractive index, size, and vertical distribution of aerosol particles during the event of intense aerosol advection in detail. For this purpose, we used the ground-based observations of the sun-photometer AERONET Nicosia station, lidar measurements, and back trajectories of air movements calculated using the Hybrid Single-Particle Lagrangian Integrated Trajectory Model (HYSPLIT). To compare with background aerosol load conditions during the year, the available data of AOD and AE were used from the observations at the Nicosia AERONET site in the 2015–2022 period. On 23–25 April 2019, strong aerosol advection over Nicosia was detected according to lidar and sun-photometer observations. On 25 April 2019, the day with the largest aerosol contamination, the AOD value exceeded 0.9 at λ = 500 nm. Analysis of the optical and microphysical characteristics during the extreme event supported that the aerosol advection consists of mainly Saharan dust particles. This assumption was confirmed by the AOD versus AE variations, single-scattering albedo, refractive index, and size distribution retrievals, as well as lidar data and HYSPLIT backward trajectories, where air masses containing dust particles came mostly from North Africa. The analysis shows that the April 2019 event was one of the strongest aerosol surges that regularly take place in springtime in the atmosphere over Cyprus. The noticeable reduction in the effective radiative forcing caused by increasing aerosol amount during the aerosol dust outbreak was revealed.

Keywords: aerosol; AERONET; lidar; aerosol advection; sun-photometer

Citation: Yukhymchuk, Y.; Milinevsky, G.; Syniavskyi, I.; Popovici, I.; Unga, F.; Sciare, J.; Marenco, F.; Pikridas, M.; Goloub, P. Atmospheric Aerosol Outbreak over Nicosia, Cyprus, in April 2019: Case Study. *Atmosphere* **2022**, *13*, 1997. https://doi.org/10.3390/atmos13121997

Academic Editors: Peng Wang, Lyudmila Mihaylova, Khan Alam, Muhammad Fahim Khokhar, Liangxiu Han and Yaxing Du

Received: 12 October 2022
Accepted: 24 November 2022
Published: 29 November 2022

1. Introduction

Aerosol particles in the atmosphere are one of the less known components of the atmosphere that impact human health and the global climate. According to the Fifth Assessment Report of the Intergovernmental Panel on Climate Change [1], aerosol–cloud interactions show the largest uncertainties reached at 0.5 Wm^{-2} in the estimating changes in the Earth's energy budget. Direct aerosol impact on the energy budget in the Earth's atmosphere occurs due to scattering and absorbing solar radiation [2–4]. The indirect effect consists of the interaction between aerosols and clouds: aerosol particles act as

cloud condensation nuclei and ice nuclei [5–7]. Aerosols can change droplet size, droplet concentration in the cloud, and alter cloud radiative properties.

There are some regions on the planet that are especially responsive to global warming and are exposed to greater risk than other regions. They are known as climate change hotspots [8]. Cyprus Island located in the Eastern Mediterranean is one of these hotspots with semi-arid climate [9–11]. Providing research at the climate hotspots is significant for understanding the climate change impact on the regions where the temperatures increase faster than in some others [1].

Cyprus is affected by a mixture of various aerosol types such as dust particles from deserts, biomass burning aerosol from North-Eastern Europe, and anthropogenic pollution from urban Southeastern Europe and, certainly, marine aerosols could be observed over the island [10]. Cyprus Island also is under high risk of forest fires. High temperatures with drought periods lead to the ignition and spreading of forest fires, particularly in summer. The highest risk is in June and July [10]. In addition to smoke particles from fires, mineral dust from the Saharan desert and deserts in the Middle East are occasionally transported to Cyprus. The particles from this area are transported for thousands of kilometers [12]. The mineral dust from the Saharan desert was detected in different parts of the world and studied in many papers. The results of the detection of mineral dust in Northern, Southern and Eastern Europe can be found in [13–16]. The contamination of the Cyprus atmosphere by Saharan dust outbreaks over Nicosia was studied by Amiridis et al. [17] and Papayannis et al. [18]. The lidar aerosol studies for the Eastern Mediterranean were presented by Nisantzi et al. [19] and Mamali et al. [20].

In this paper, we study the event of intense aerosol advection over the Cyprus area, which took place on 23–25 April 2019. Our analysis is based on sun-photometer and lidar observations accompanied by HYSPLIT backward trajectories calculations. Section 2 describes the instruments and methods used in the work. Section 3 contains the observation results, backward trajectories calculations, and discussion, followed by conclusions in Section 4.

2. Data and Methods

2.1. AERONET Sun-Photometer Station

The international network of automatic AERONET (AErosol RObotic NETwork) CIMEL CE318 sun-photometers [21] is one of the most advanced remote sensing aerosol monitoring systems [22–24]. The AERONET network is operated by NASA (USA), and the French and Spanish ACTRIS (Aerosols Clouds and TRace gas InfraStructure) components in Europe, and includes several hundred stations (about ~600) around the world. The tools of this network allow obtaining long-term series for the accurate aerosol parameters that can be used for the analysis of the aerosol particle variations [25–27], studying the seasonal dynamics and the local aerosol behavior.

Accuracy of aerosol retrievals are about ~0.01 ($\lambda > 440$ nm) for aerosol optical depth (AOD) provided by the AERONET network, depending on sun-photometer calibration [28]. The calibration consists of two parts: AOD and sky radiance measurements [29,30]. Direct Sun Calibration includes the determination of the calibration coefficients. These coefficients are needed to convert the instrument digital output to the desired scientific output. For aerosol parameter analysis in this paper, we use the aerosol Version 2 direct sun algorithm [29] level 1.5 and level 2.0 parameters from the AERONET database: daily data, daily averages of AOD at 440, 500, and 870 nm, and the Ångström exponent (AE) values computed using the 440 and 870 nm spectral channels, refractive index (RI), and single-scattering albedo (SSA). For the April 2019 event analysis and for AOD and AE consideration in the period from 2015 till spring 2021, the data level 2.0 was used. From summer 2021 till the autumn 2022, only the data level 1.5 was available.

The sun-photometer used in this study is located at the Cyprus Atmospheric Observatory in Nicosia (CAO-Nicosia, Figure 1) at the premises of the Cyprus Institute, Athalassa

campus, in Aglantzia [31], ~5 km from the Nicosia city center. The station is equipped with the CE318NE sun-photometer from Cimel Electronique [21].

Figure 1. Location of the AERONET station Nicosia at the Cyprus Atmospheric Observatory (CAO) station (35.1406° N, 33.3814° E, 181 m a.s.l.) in Nicosia, Cyprus [31].

2.2. Lidar Measurements

The lidar (Light Detection and Ranging) measurement was used to retrieve altitude distribution and properties of atmospheric aerosol [32]. The Cimel Electronique CE370 micropulse lidar [33] was co-located with the sun-photometer in the period 2018–2020. The CE370 lidar is a mono-wavelength elastic lidar operating at 532 nm, with no polarization channel. This instrument allows monitoring of aerosols and clouds in the troposphere with a vertical resolution of 15 m and usually up to 15 km. During moderate aerosol loadings, lidar observations could reach altitudes of about 15–20 km. The design of CE370 consists of a shared transmitter–receiver telescope (mono-axis system) connected to the control and acquisition unit through the optical fiber [33]. Combining automatic sun-photometer and lidar data is the significant approach that allows retrieving extinction, lidar ratio, and mass concentration. In addition, the near-real-time (NRT) processing chain combining photometer (day and night) and lidar data for retrieval of the just-mentioned parameters is being implemented in the ACTRIS-France data center. In this work, we use data of CE370 lidar, which were available at Nicosia during the 2018–2020 period.

2.3. HYSPLIT Model

The Hybrid Single-Particle Lagrangian Integrated Trajectory model (HYSPLIT, [34]) is one of the most widely used models for calculations of atmospheric air masses' backward trajectories. The model calculation method is a hybrid between the Lagrangian approach (calculations of the trajectories or air move) and the Eulerian methodology (connected with computing air pollutants) [35]. HYSPLIT can use a large variety of meteorological model data in its calculations, ranging from mesoscale to global scales. The calculation of forward and backward trajectories allows studying the transport of pollutants over different spatial and temporal ranges [35].

In our research, for backward trajectory building, we use the HYSPLIT model with the meteorological data files from The National Oceanic and Atmospheric Administration (NOAA) Global Data Assimilation System (GDAS). GDAS contains different meteorological data such as surface observations, satellite observations, wind profiler data, balloon data, radar observations, and aircraft reports. The NOAA Global Forecast System (GFS) model used GDAS to place observations into a gridded model space for starting or initializing weather forecasts with observed data [36].

3. Results and Discussion

This section contains the observation results and analyses of the optical and microphysical properties of aerosols particles by sun-photometer measurements of the AERONET network (Section 3.1), spatial distribution of aerosols particles in the atmosphere over Nicosia (Cyprus) by lidar sensing (Section 3.2), backward air mass transport trajectories made using HYSPLIT model (Section 3.3), and evaluation of effective aerosol forcing (Section 3.4).

3.1. AERONET Sun-Photometer Observations

3.1.1. Optical Characteristics of Aerosol Particles over 2015–2022

To evaluate the level of the April 2019 aerosol outbreak event over Nicosia, the available data on the state of aerosol contamination for the 2015–2022 period by sun-photometer observations were reviewed. We used AOD as a measure of the total amount of aerosols in the atmospheric column. Single-scattering albedo (SSA) and Ångström exponent (AE) strongly depend on intensive aerosol properties and can be used to make assumptions on the aerosol type. The AERONET site in Nicosia has provided observations on a nearly continuous basis since February 2019. Some observations at this site are also available for March–April 2015 and April 2016. The aerosol optical depth reported by this instrument and Ångström exponent are shown in Figure 2.

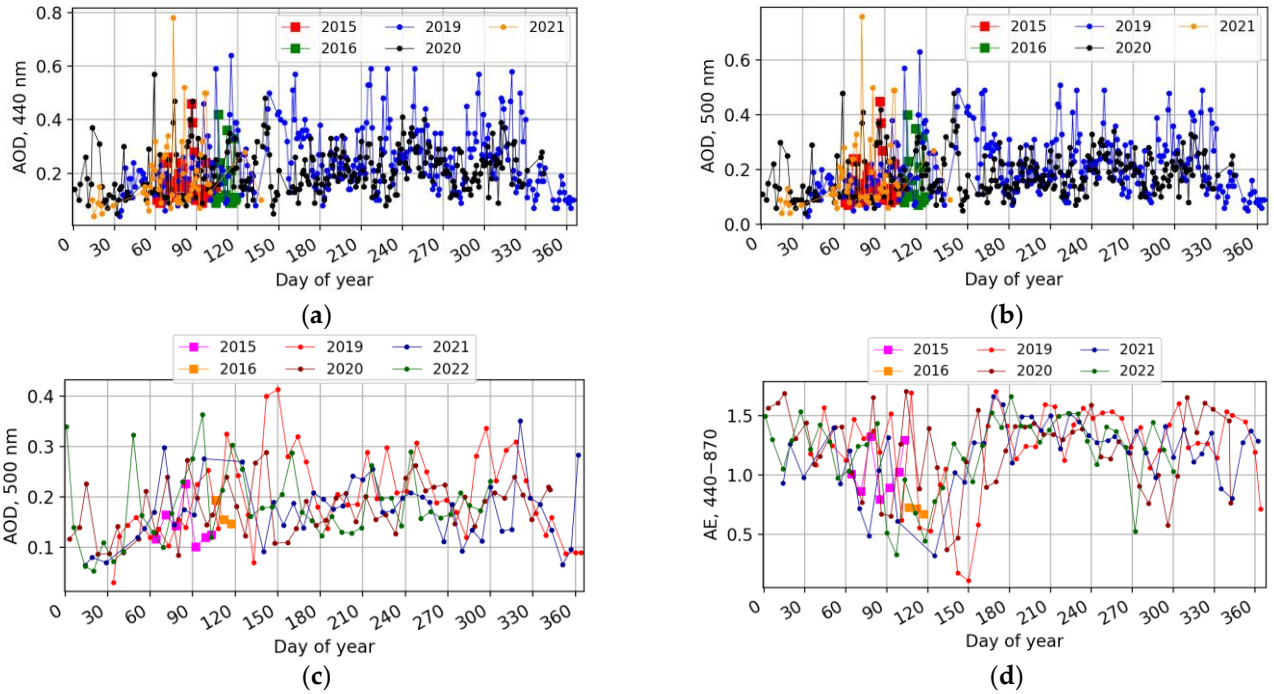

Figure 2. Aerosol optical depth and Ångström exponent during the 2015–2022 period; (**a**) AOD (440 nm) and (**b**) AOD (500 nm) daily mean data; (**c**) AOD (500 nm) and (**d**) AE (440–870 nm) weekly mean data. The AERONET sun-photometer data (**a**,**b**) level 2.0 (2015–2021) and level 1.5 (2021–2022); see details in the text. Data in (**c**,**d**) level 2.0 (2015–2019) and level 1.5 (2020–2022).

The seasonal variation of AOD in the atmosphere over Nicosia shows the lowest concentration of aerosol particles during the winter season (typically less than 0.1 in 440 and 500 nm). From the beginning of spring, AOD values start to increase and vary until the end of autumn, reaching ~0.25 (440 nm) and ~0.20 (500 nm) on average, with sporadic episodes when values up to ~0.6 (440 nm) and ~0.5 (500 nm) are reported. In spring months, the large aerosol intrusion is seen with AOD values ~0.6–0.8 (500 nm) almost each year. Furthermore, in March–April 2015 and April 2016, the AOD values were smaller (~0.15) than in the same period of 2019–2021 (~0.25). In Figure 2a,b, data for 2021 at level 2.0 is

available only for the winter–spring period, for the rest of 2021 and for 2022—the data level was 1.5.

The Ångström exponent demonstrates the dominant size particles during observations. The computation of AE requires AOD at different wavelengths. This value shows the connection between aerosol optical depth and their spectral dependence. AE depends on the size of particles, when larger AE values correspond to finer particles, and it is one of the main characteristics of different aerosol types. The seasonal variations of the AE (440–870 nm) daily mean and weekly averaged values are shown in Figure 2d. During the 2019–2022 period, the AOD and AE variations have a similar behavior with some seasonal dependence. The AE data exhibit seasonal variations when the AE decrease was observed from the middle of spring to the beginning of summer (Figure 2d). This period in Nicosia usually corresponds to the transport of mineral dust from the Sahara Desert to East Mediterranean areas (see, e.g., [17,18]). In comparison with other spring aerosol increases, the April 2019 aerosol transfer event was one of the largest, when AE (470–870 nm) dropped below 0.3 in correspondence with increases in single AOD (500 nm) above 0.9, which suggests a strong dust intrusion.

3.1.2. Study of the April 2019 Event

The increased daily average AOD value at 500 nm ~0.7 was observed on 25 April 2019. During 23–25 April 2019, the AOD (500 nm) varied from ~0.1 to ~0.9, when single measurements during the day showed an AOD (500 nm) value up to ~0.98 (Figure 3b, brown line). The increasing AOD and simultaneously decreasing AE indicate the arrival of a significant aerosol load and changes in the aerosol particle properties in the atmosphere over Nicosia.

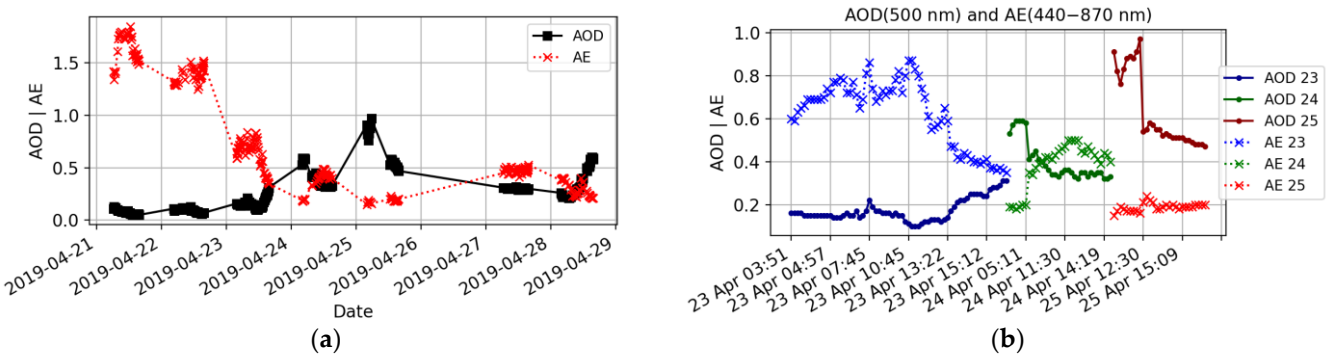

Figure 3. Changes in aerosol optical depth (AOD 500 nm) and Ångström exponent (AE 470–870 nm) during (**a**) the 21–29 April period and (**b**) day time of 23–25 April 2019, Nicosia, Cyprus. Data level 2.0.

Moreover, the AE value change, which decreased from 0.7 to less than 0.2, suggests that this is due to the advection of mineral dust that started to arrive at the end of 23 April (Figure 3). The AE variations anticorrelate with the AOD values (Figure 3). The light blue line shows that the AE decreased from 0.6–0.8 to $\leq$0.4 on 23 April. On 25 April, a sun-photometer detected the lowest AE values of $\leq$0.2 (the pink curve in Figure 3b).

SSA depends on absorbing and scattering characteristics of aerosol particles. In Figure 4a the change from absorbing aerosols to aerosols with mostly scattering properties is clearly seen in transition from 21–22 April to 23–25 April. Moreover, this gradual change in the aerosol properties from absorbing to the scattering particles is observed with a sequential transition from day to day. According to data in Figure 4, the highest SSA values were detected on 25 April 2019, which were >0.99 (675–1020 nm) at 4:46 a.m. UTC (Figure 4b, blue line). Note that the SSA data level 2.0 is very close to SSA calculation level 1.5 on 25 April.

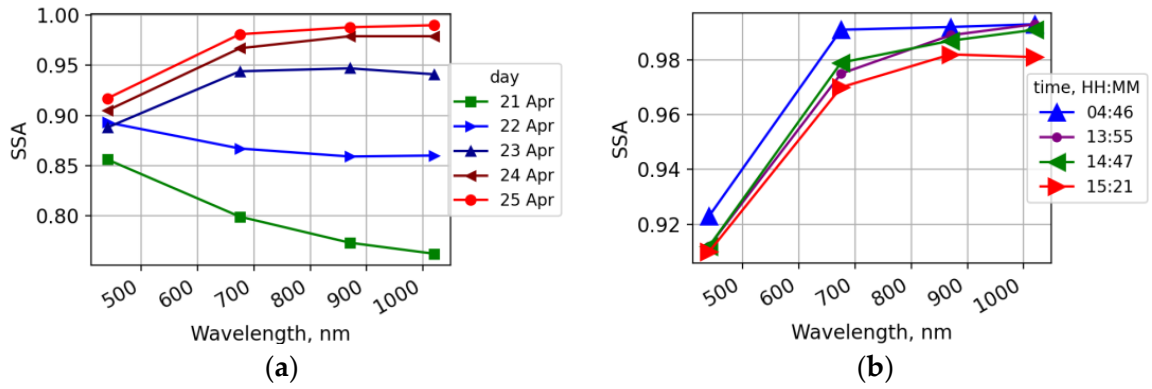

Figure 4. The single-scattering albedo (SSA) (**a**) 21–25 April and during the day of (**b**) 25 April 2019. Data level 1.5 for (**a**) 21–25 April and level 2.0 for (**b**) 25 April.

3.1.3. Microphysical Characteristics of Aerosol Particles

In this section, we consider microphysical aerosol characteristics: size distribution and refractive index. These properties can be obtained using a joint sun-photometer AOD and radiance inversion scheme [25] operationally applied in the AERONET network.

Aerosol particles have a quite wide range of sizes: from the smallest with tens of nanometers to the largest with a size of hundreds of micrometers. Conditionally, the whole aerosol fraction could be separated into coarse (diameter > 1 μm) and fine modes (diameter < 1 μm). Each mode can correspond to a different aerosol type. According to size distribution variation during the 21–28 April period, the gradual increasing in coarse-mode particles amount is observed from 21 to 25 April (Figure 5a) and similarly decreasing from 25 to 27–28 April (Figure 5b). During the aerosol outbreak event, the coarse mode was most dominant on 25 April 2019. In Figure 5, the large proportion of aerosols varies in size, ranging from 1 to 10 μm, with the highest values in the morning of 25 April. The size distribution shape with the dominated coarse mode is typical for mineral dust advection [37,38].

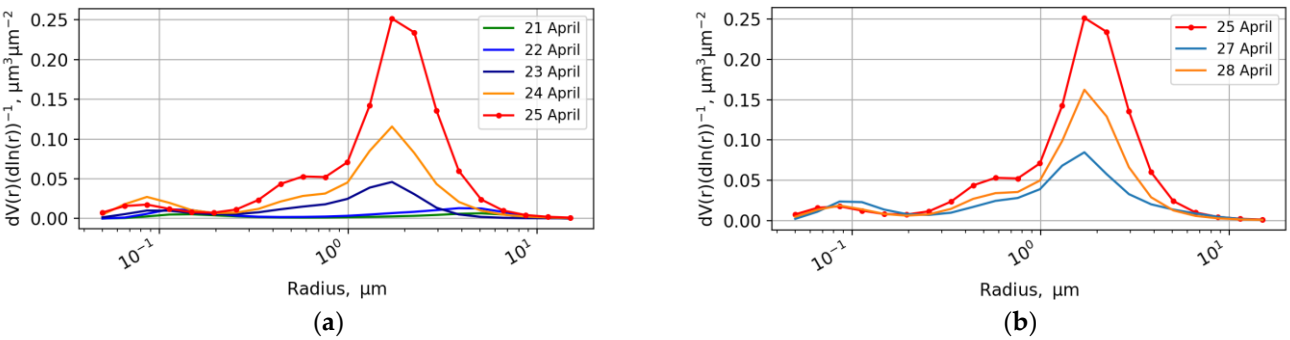

Figure 5. Aerosol volume size distribution on (**a**) 21–25 April and (**b**) 25–28 April 2019. Data level 2.0. Data on 26 April are not available.

The refractive index (RI) of aerosol particles (real and imaginary parts) is associated with the particles' composition. The scattering aerosol property impacts the real part, and the absorbing ability is responsible for the imaginary part of refractive index values. The AERONET data of both parts of the refractive index for 25 April 2019 are presented in Figure 6. The RI real part values are in the range of 1.43–1.52 (Figure 6a); the values and variations with wavelengths are typical for mineral dust particles [38]. A similar result is obtained for the RI imaginary part. Firstly, the RI imaginary part is in a range less than 0.004 (Figure 6b), which is typical for Sahara dust particles [39]. Secondly, the shape of the variations of the RI imaginary part with wavelengths describes the changes matched with mineral dust [38].

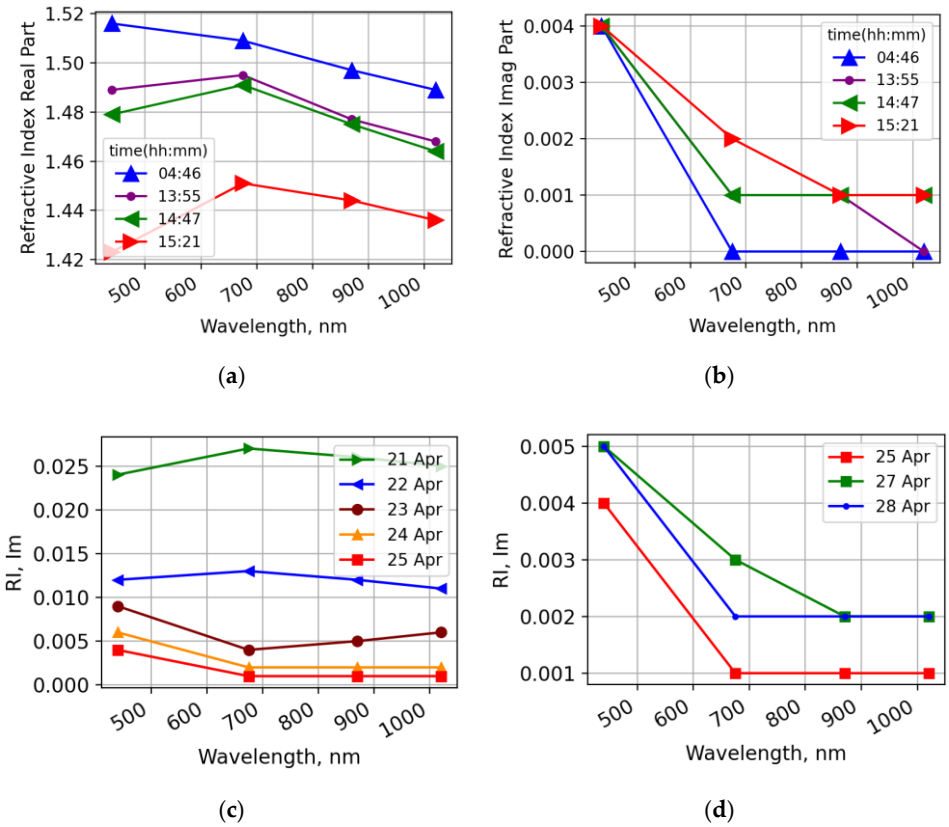

Figure 6. Refractive index: (**a**) real part, (**b**) imaginary part on 25 April 2019, data level 2.0; imaginary part (**c**) 25 April 2019, (**d**) 25, 27, 28 April 2019, data level 1.5. RI values on 26 April 2019 are not available.

3.1.4. Cluster Analysis for Aerosols Particle Types

The cluster analysis method allows to group data in datasets with similar characteristics. In the case of the 23–25 April events, we have enough AOD and AE measurements to provide the cluster analysis of aerosol-type particles [40,41]. The changes in aerosol types are shown in the scatter plot AOD versus AE in Figure 7. The image shows the changes in dominant aerosol type in the atmosphere over Nicosia. During two days, the mostly anthropogenic type of aerosol was switched to the aerosol with mineral dust features. This transition took place quickly but smoothly; therefore, the contamination was not spontaneous and could be moved over Nicosia with air mass transport from distant sources.

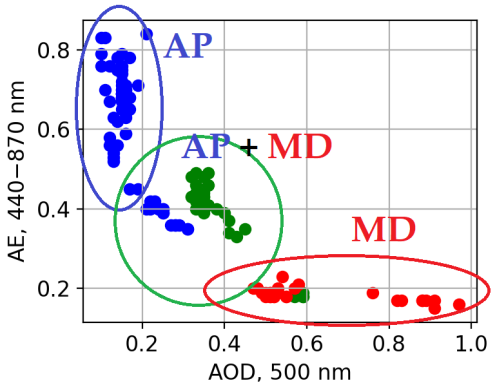

Figure 7. Scatter plot for aerosol optical depth (500 nm) versus Ångström exponent (440–870 nm) dependency during 23–25 April 2019: blue dots—23 April, green—24 April, and red—25 April. AP—anthropogenic aerosol particles; MD—mineral dust. Data level 2.0.

3.2. Lidar Observations during 25 April 2019

Lidar observations provide information on the altitude distribution of aerosol particles with high spatial resolution. In contrast to AERONET observations, which retrieve aerosol characteristics for a whole atmospheric column, lidar observations allow defining the altitudes of particles' spatial structure [18].

This information is important for studying aerosol dynamics over some territories, aerosol properties, and sources of aerosol particles. The main part of aerosol advection is concentrated at the planetary boundary level, usually at the altitudes below 1000–2000 m, depending on the topography [42,43]. The smoke and biomass burning aerosol from powerful wildfires can rise to higher altitudes, such as 4–5 km, and ash from volcano eruptions could be able to reach the stratosphere [44,45].

In the case of Nicosia, lidar observations cover the entire year of 2019, including the period of the event of 23–25 April 2019. Based on lidar measurements and AERONET sun-photometer data, we provided analysis of the aerosol dust contamination over Nicosia on 25 April 2019. As was mentioned before, the combination of sun-photometer and lidar data allowed retrieving extinction, lidar ratio, and mass concentration during aerosol outbreak events. Figure 8 presents the lidar time series of range-corrected backscatter signal for Nicosia on 25 April 2019. On 23 April, the lidar observations showed a low amount of aerosol particles in the atmosphere, and on the next day, the backscatter signal increased. The maximum backscattering was detected on 25 April.

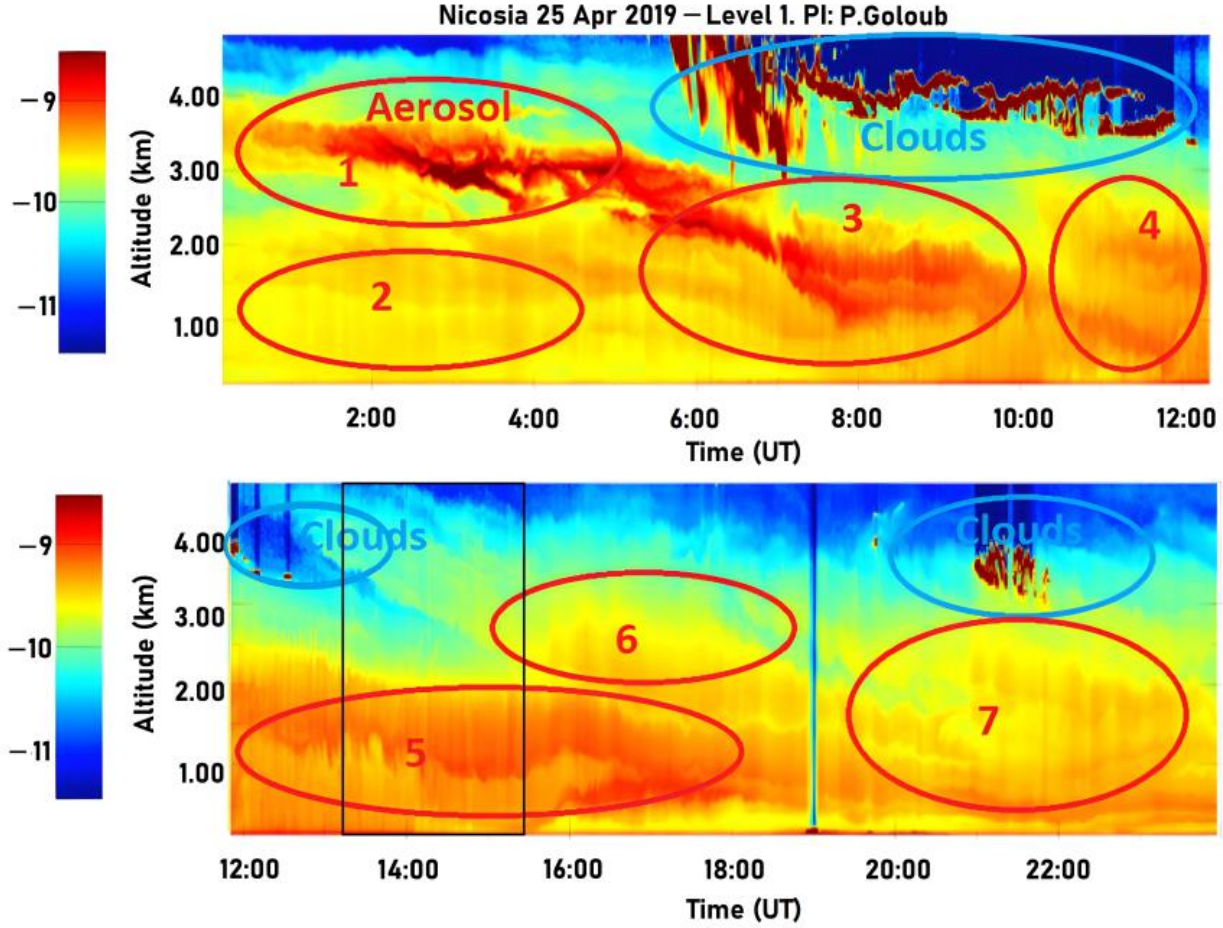

Figure 8. Lidar time series of range-corrected backscatter signal (in arbitrary unit) for Nicosia, Cyprus, 25 April 2019. Blue circles indicate the clouds, and red circles and numbers (1–7) mark the aerosol layers.

We considered the lidar observations on 25 April in detail, because it was the day with the most dust load in the 23–25 April 2019 period. Backscatter signals according to

lidar observations started to grow up on 24 April. When a new aerosol plume arrived at high altitudes (3.5 km, the layer 1 at -1 h on 25 April, Figure 8), there was already aerosol advection below 2 km (Figure 8, the layer 2). The upcoming aerosol layer 1 was located at altitudes between 3 and 4 km. At 5 h, aerosol layer 1 decreased its altitude and mixed with layer 2, forming layer 3 (Figure 8, the layer 3). The layer 5 (former layer 4) was dominant until 16 h. Then, it was separated into layers 6 and 7, which were less dense than layer 5 (Figure 8, layer 5). This atmospheric dynamic is probably due to atmospheric advection, the details of which are not a topic of this study.

In order to determine the aerosol vertical profile of the extinction coefficient and mass concentration using lidar data, the different models of aerosol types and their size distribution should be used. In the AERONET retrieval algorithm, aerosol types are modeled by several modes with a certain aerosol particle size distribution, where each mode is a mixture of homogeneous spherical particles and randomly oriented spheroids [24,26].

Retrieval of extinction profile and effective lidar ratio (the extinction to backscattering ratio) are performed during daytime using methodology [46] that is based on the Klett and Fernald solution [47,48] using the BASIC algorithm [49,50], and it includes the use of the accurate AOD measurements, such as AERONET. The other AERONET observed aerosol characteristics are the particle diameter (for two modes), the proportion of fine and coarse mode, particle density, and real and imaginary parts of the refractive index, which, in synergy with the extinction profile, could be used for the calculation of aerosol mass concentration [49]. The lidar retrieval algorithm allows choosing the aerosol type model based on the above-mentioned aerosol properties: biomass burning, ash, urban–industrial, dust, sea salt, or manually defining.

The extinction profiles in 25 April 2019 are presented in Figure 9c. For comparison, on undisturbed days the extinction profiles on 21 April 2019 were calculated (Figure 9a). According to aerosol dynamics, the extinction profiles (Figure 9c) are affected by aerosol plum in the atmosphere without cloud impact. On 25 April, the extinction coefficient varied from 0.05 to 0.2 km^{-1}. For mass concentration calculations, the following assumptions and observations were used: (1) refractive index from AERONET observations(Section 3.1, Figure 6); (2) the mineral dust density approximately 2.6 g m^{-3} [51,52]; (3) the dust model for aerosol particle distribution (according to AERONET observations of aerosol size distribution in Figure 5 in Section 3.1, the dust model is the best for this case); and (4) lidar extinction measurements. The result of the aerosol mass concentration that corresponds to extinction 0.6 is more than 1000 μg m^{-3}. With assumptions that the average particle radius is 1.3 μm (Figure 5), the calculated average mass concentration is in the range 100–300 μg m^{-3} (Figure 9d). In comparison with the "background" day 21 April, the largest value of mass concentration (300 μg m^{-3}) exceeds background data by more than 10 times (27 μg m^{-3}); compare Figures 9b and 9d. Two peaks of mass concentration at around ~1.5 and ~3.5 km (Figure 9d) correspond to aerosol plumes at layers 5 and 6 in Figure 8.

3.3. HYSPLIT Calculation of Air Mass Transport and MODIS Observations

For air mass movement calculation, the HYSPLIT model uses meteorological data files from the Global Data Assimilation System (GDAS), which includes a variety of data from different instruments and sources of data: satellite, ground-based, and aircraft measurements [36]. To study the impact of air mass transport from different regions to Nicosia, the calculations of backward trajectories for different periods and trajectory frequency have been provided. The 6-day backward trajectories are presented in Figure 10a.

The trajectory starts every 12 h and runs for 72 h. That means the latest curve (red) starts at the same time when the earliest (yellow) ends. The altitude for calculation is 500 m above ground level (AGL). The results show the changes in the air mass transport direction from East Europe on 21–24 April to North Africa on 24–25 April. The frequency calculation provides specific information about dominant wind directions and air mass movements over Nicosia. The trajectory frequency option starts a trajectory from a single location

(Nicosia) at the height of 500 m AGL every 3 h. The duration of 72 h in 3 days for every trajectory is the same as in the previous backward trajectory calculation (Figure 10b).

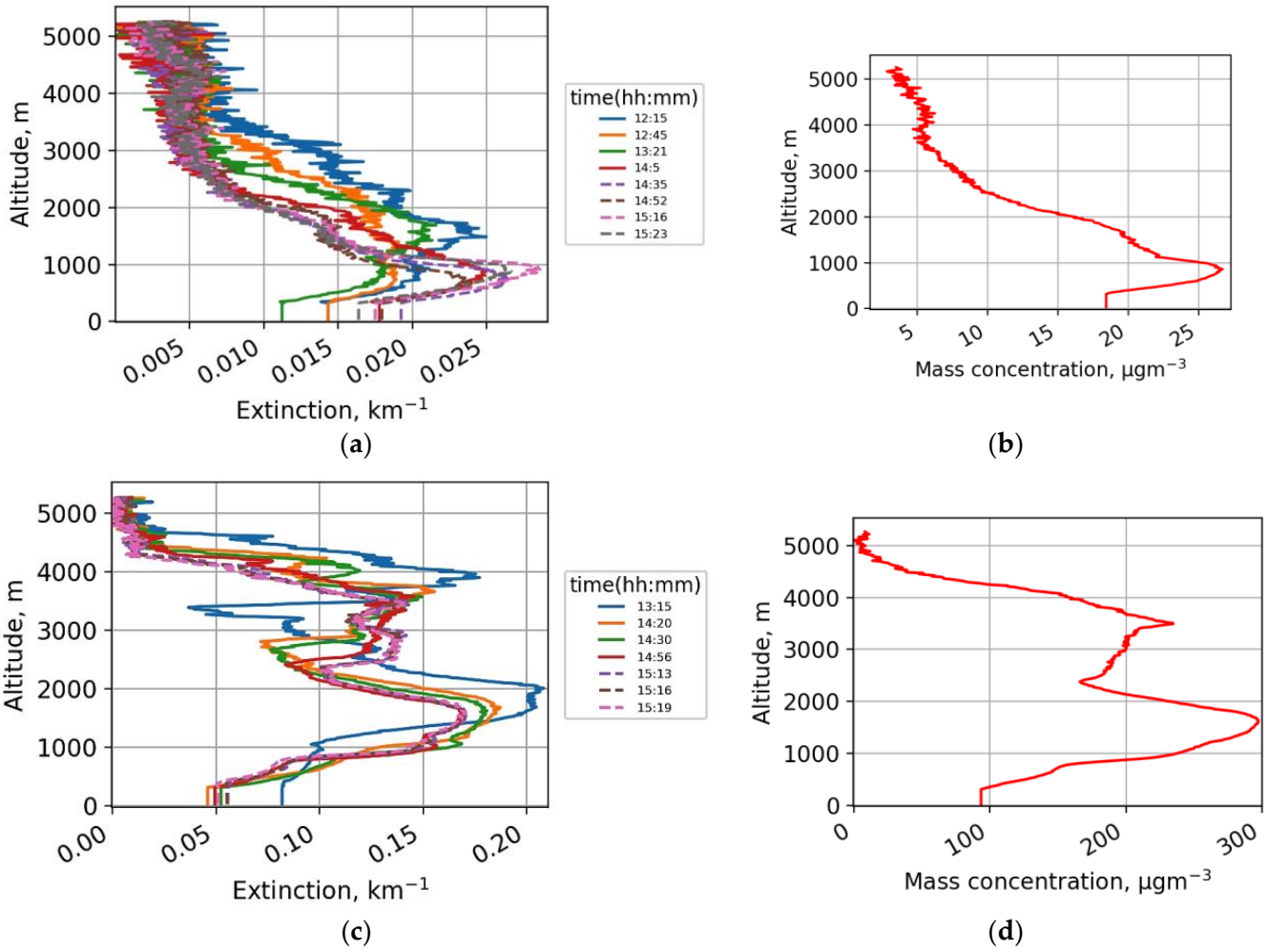

Figure 9. Extinction altitude profiles on (**a**) 21 April in the period from 12 h 15 m until 15 h 23 m and (**c**) 25 April in the period from 13 h 15 m until 15 h 19 m; average mass concentration altitude profiles on (**b**) 21 April and (**d**) 25 April in the atmosphere over Nicosia.

The main part of the upcoming aerosol particles was located at an altitude of less than 4 km. Figure 11a presents the backward trajectories for three different altitudes: 100, 500, and 1000 m AGL. The red and blue lines correspond to 100 and 500 m, accordingly, almost matching the results in Figure 10a. For higher altitudes (1000 m, green line, Figure 10a), the trajectory is located at the western part in comparison with the 100 and 500 m trajectories. Trajectories for the 3 previous days before 25 April start over Libya and Egypt, which include the territory of the Sahara Desert (Figures 10 and 11a).

In the Aqua/MODIS satellite image (Figure 11b) [53], the haze of the dust is visible over the territory of Egypt and the eastern part on the Mediterranean Sea including Cyprus. This haze corresponds to mineral dust particles transported from the Sahara Desert. Comparison with the results of the HYSPLIT calculation confirmed that mineral dust came to Nicosia with air masses transported from the Sahara Desert region.

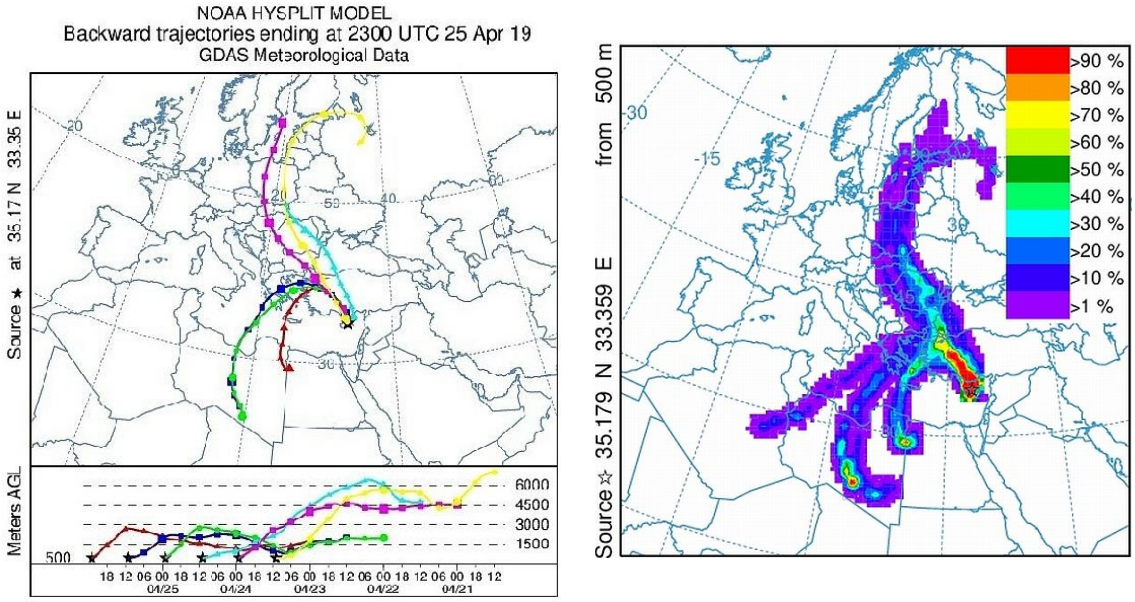

(**a**) (**b**)

Figure 10. (**a**) Backward trajectory of the air mass at 23 UTC and (**b**) trajectory frequency (**b**) on 25 April 2019, Nicosia, Cyprus. HYSPLIT calculation. Different colors at the bottom scale of vertical air movements at (**a**) correspond to different air mass trajectory for a particular day that comes from a calculated altitude to altitude of 500 m (AGL). For example, the yellow line shows air moving from an altitude above 6000 m (AGL) that comes by trajectory (marked on the map the same color) and was detected at Nicosia at an altitude of 500 m AGL at 12 h on 23 April. Red color corresponds to 00 h on 26 April, blue—to 12 h on 25 April, green—to 00 h on 25 April, light blue—to 12 h on 24 April, and pink—to 00 h on 24 April.

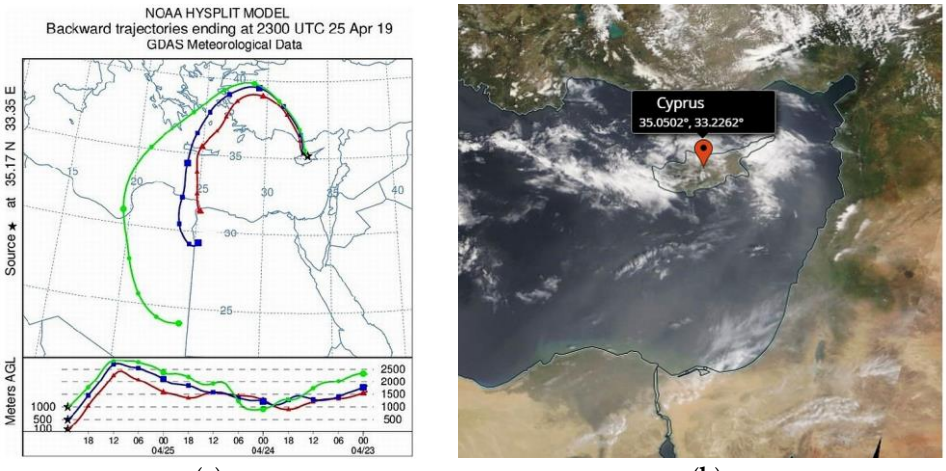

(**a**) (**b**)

Figure 11. (**a**) Backward trajectory of the air mass movement at 23 UTC: red trajectory corresponds to air mass transport that started at an altitude of 1500 m AGL at 00 h on 23 April and finished at 100 m (AGL) at Nicosia, blue—came from around 2000 m AGL to 500 m AGL and green—from 2500 to 1000 m AGL (map shows the horizontal movement and scale at the bottom the vertical movements of air mass), and (**b**) Aqua/MODIS image on 25 April 2019 [53], Cyprus, Eastern Mediterranean.

3.4. Effective Radiative Forcing Evaluation

Radiative forcing (RF) and effective radiative forcing (ERF) are the measure of the net change in the Earth system's energy balance due to changes in different atmospheric constituents. RF is defined as the difference in net downward flux (shortwave + longwave) at the tropopause after obtaining the stratospheric temperatures to radiative equilibrium [1].

That means RF does not include the impact of short-term changes in the atmosphere. The ERF concept allows estimating an influence of rapid changes for all atmospheric variables including aerosols [1]. The RF and ERF daily averaged values were retrieved from the AERONET website for the period 21–29 April when the discussed aerosol outbreak took place [24]. At the top of the atmosphere, RF and ERF changes have similar dynamics: in both cases, after 21 April, they start to decrease (see Figure 12a). RF values changed from ~0 Wm^{-2} on 21 April to −38 Wm^{-2} on 25 April, and then slightly increased.

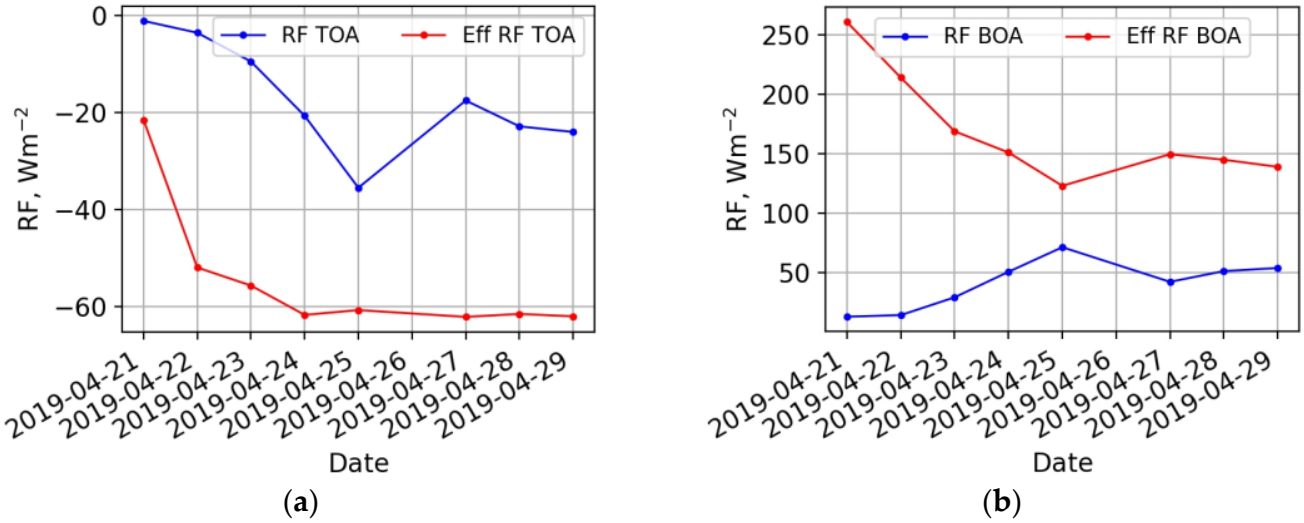

Figure 12. Radiative forcing (RF) and effective radiative forcing (Eff RF) at (**a**) the top of atmosphere (TOA), (**b**) bottom of atmosphere (BOA), and daily averaged RF data in the 21–29 April period. AERONET retrieval data level 2.0 for (**b**).

In the case of ERF on 21 April, the value from about −21 Wm^{-2} changed to less than −60 Wm^{-2} in the following days of the aerosol outbreak period. Decreasing RF and ERF mean cooling at the top of the atmosphere due to aerosol amount increase. The ERF variations at the bottom of the atmosphere have a similar behavior (Figure 12b). EFR values decreased from more than 250 Wm^{-2} outside of the aerosol outbreak to 125 Wm^{-2} on the day of the highest contamination, 25 April. The aerosol outbreak resulted in less income energy from the top of the atmosphere due to air contamination and led to decreasing EFR and cooling.

4. Conclusions

The results of detailed analysis of the intensive aerosol plume event over Nicosia, Cyprus in the Eastern Mediterranean in April 2019 are presented in this paper. The characteristics of aerosol particles during the high atmospheric aerosol contamination event are considered. For analysis, the data from the sun-photometer Nicosia AERONET station, the ground-based automatic micro-lidar, and the HYSPLIT back trajectories were used. We compare the aerosol characteristics during the April 2019 event with aerosol parameters outside of this period of strong contamination AOD (500 nm), AOD (440 nm), and AE (440–870 nm) on the basis of the available AERONET data in the years 2015–2022. This comparison reveals that a similar event takes place almost every spring, and the considered aerosol outbreak was one of the strongest. The AOD exhibits seasonal variation, with the lowest concentration of aerosol particles during the winter season (AOD < 0.1) and increasing values in spring. Day-by-day analysis several days before, during, and after the outbreak event shows gradual changes in aerosol characteristics—AE, SSA, aerosol size distribution and refractive index (see Figures 3–6) from fine-mode to coarse-mode particles, and from absorbing to mostly scattering aerosols. The scatter plot of AOD versus AE values also shows transition from the mostly anthropogenic type of aerosol to mineral dust (Figure 7).

According to lidar data, the extinction altitude profiles and average mass concentration altitude profiles have been changed dramatically from "background" conditions to the event of aerosol contamination (Figure 9). The largest value of mass concentration during the event by lidar profiles is about 300 μg m^{-3}, which exceeds background data by more than 10 times, and two peaks in the mass concentration profile are seen at ~1.5 and ~3.5 km instead of the usual single, much smaller maximum below ~1.0 km. All these aerosol parameters, AOD, Ångström exponent, single-scattering albedo, refractive index, and size distribution, suggest the arrival in the atmosphere over Nicosia in April 2019 of the large amount of mineral dust particles, with AOD at least five times larger (~0.9 at 500 nm, see Figure 3) than background values (~0.2). The backward trajectory analysis clearly shows that the mineral dust arrived from the Sahara Desert region and Egypt. The mineral dust aerosol properties in the extreme event of 25 April 2019 were confirmed by lidar measurements and retrievals, scatter plot analysis, and aerosol volume size distribution.

The aerosol conditions in the region around Cyprus were studied in previous works [10,54–56]. Our analysis and previous studies show that the mineral dust of the Saharan Desert from the southwest and of the Arabian Peninsula Desert from the southeast was often transported to the atmosphere over Cyprus in several events since 2015. The 23–25 April 2019 event was one of the extreme aerosol outbreaks by mineral dust from the Saharan Desert in the atmosphere over Cyprus. We evaluated the assumption of how this type of aerosol outbreak can impact radiative forcing in the region using the AERONET approach [24]. Results show noticeable reduction in the effective radiative forcing caused by increasing aerosol amounts during the outbreak. These results can be used to quantify the impact of aerosol dust as a forcing agent that induces rapid changes in regional radiative forcing in the atmosphere.

Author Contributions: Conceptualization, Y.Y. and P.G.; methodology, Y.Y., P.G. and G.M.; software, Y.Y.; validation, Y.Y., P.G., I.P. and G.M.; investigation, Y.Y., P.G., I.S., I.P., J.S., M.P., F.M., F.U. and G.M.; writing—original draft preparation, G.M., M.P., P.G. and Y.Y.; writing—review and editing, G.M., I.S., P.G., I.P., J.S., M.P., F.U. and Y.Y.; visualization, Y.Y.; supervision, J.S., G.M. and P.G.; project administration, G.M., I.P. and P.G. Each author contributed to the interpretation and discussion of the results and edited the manuscript. All authors have read and agreed to the published version of the manuscript.

Funding: This work was partly supported by the Space Program for 2018–2022 of the National Academy of Sciences of Ukraine through the project 03/22, Ukraine; by Ministry of Education and Science of Ukraine, Kyiv, through the projects 20BF051-02 and BF/30-2021; by College of Physics International Center of Future Science, Jilin University, China. The work was partly supported by the European Union's Horizon 2020 research and innovation program under the Marie Skłodowska-Curie grant agreement No 778349 GRASP-ACE and research and innovation program under ACTRIS-2 grant agreement No 654109.

Institutional Review Board Statement: Not applicable.

Informed Consent Statement: Not applicable.

Data Availability Statement: Not applicable.

Acknowledgments: We thank Brent Holben (NASA/GSFC) for managing the AERONET program and its sites. The authors also acknowledge the Climate and Atmosphere Research Centre (CARE-C), Cyprus station, Nicosia, Cyprus. The high quality AERONET/PHOTONS data were provided by the CIMEL sun-photometer calibration performed at the AERONET-EUROPE calibration center. The authors also would like to acknowledge the European Commission Horizon 2020 Program that funded the ERA-PLANET/SMURBS project.

Conflicts of Interest: The authors declare no conflict of interest.

References

1. IPCC. *Climate Change 2022: Impacts, Adaptation, and Vulnerability. Contribution of Working Group II to the Sixth Assessment Report of the Intergovernmental Panel on Climate Change*; Pörtner, H.-O., Roberts, D.C., Tignor, M., Poloczanska, E.S., Mintenbeck, K., Alegría, A., Craig, M., Langsdorf, S., Löschke, S., Möller, V., et al., Eds.; Cambridge University Press: Cambridge, UK; New York, NY, USA, 2022; Available online: https://www.ipcc.ch/report/ar6/wg2/ (accessed on 20 March 2022).
2. Li, L.; Mahowald, N.M.; Miller, R.L.; Pérez García-Pando, C.; Klose, M.; Hamilton, D.S.; Gonçalves Ageitos, M.; Ginoux, P.; Balkanski, Y.; Green, R.O.; et al. Quantifying the range of the dust direct radiative effect due to source mineralogy uncertainty. *Atmos. Chem. Phys.* **2021**, *21*, 3973–4005. [CrossRef]
3. Sokolik, I.N.; Toon, O.B. Direct radiative forcing by anthropogenic airborne mineral aerosols. *Nature* **1996**, *381*, 681–683. [CrossRef]
4. Li, L.; Sokolik, I.N. The Dust Direct Radiative Impact and Its Sensitivity to the Land Surface State and Key Minerals in the WRF-Chem-DuMo Model: A Case Study of Dust Storms in Central Asia. *J. Geophys. Res. Atmos.* **2018**, *123*, 4564–4582. [CrossRef]
5. Lohmann, U.; Feichter, J. Global indirect aerosol effects: A review. *Atmos. Chem. Phys.* **2005**, *5*, 715–737. [CrossRef]
6. DeMott, P.J.; Sassen, K.; Poellot, M.R.; Baumgardner, D.; Rogers, D.C.; Brooks, S.D.; Prenni, A.J.; Kreidenweis, S.M. African dust aerosols as atmospheric ice nuclei. *Geophys. Res. Lett.* **2003**, *30*, 1732. [CrossRef]
7. Connolly, P.J.; Möhler, O.; Field, P.R.; Saathoff, H.; Burgess, R.; Choularton, T.; Gallagher, M. Studies of heterogeneous freezing by three different desert dust samples. *Atmos. Chem. Phys.* **2009**, *9*, 2805–2824. [CrossRef]
8. Fan, X.; Miao, C.; Duan, Q.; Shen, C.; Wu, Y. Future climate change hotspots under different 21st century warming scenarios. *Earth's Future* **2021**, *9*, e2021EF002027. [CrossRef]
9. Zachariadis, T. Climate Change in Cyprus: Impacts and Adaptation Policies. *Cyprus Econ. Policy Rev.* **2012**, *6*, 21–37.
10. Kaduk, C. Characterization of the Optical Properties of Complex Aerosol Mixtures Observed with a Multiwavelength-Raman-Polarization Lidar during the 6-Weeks BACCHUS Campaign in Cyprus in Spring 2015. Fakultät für Physik und Geowissenschaften der Universität Leipzig Studiengang Meteorologie, Masterarbeit 2017. Available online: https://www.tropos.de/fileadmin/user_upload/Institut/Abteilungen/Fernerkundung/Daten_PDF/MA_Clara_Kaduk.pdf (accessed on 22 April 2022).
11. Climate Data for Cities Worldwide. Available online: https://en.climate-data.org/ (accessed on 18 March 2022).
12. Prospero, J.M. Long-term measurements of the transport of African mineral dust to the southeastern United States: Implications for regional air quality. *J. Geophys. Res.* **1999**, *104*, 15917–15927. [CrossRef]
13. Ansmann, A.; Bösenberg, J.; Chaikovsky, A.; Comerón, A.; Eckhardt, S.; Eixmann, R.; Freudenthaler, V.; Ginoux, P.; Komguem, L.; Linne, H.; et al. Long-range transport of Saharan dust to northern Europe: The 11–16 October 2001 outbreak observed with EARLINET. *J. Geophys. Res.-Atmos.* **2003**, *108*, 4783. [CrossRef]
14. Wagner, F.; Bortoli, D.; Pereira, S.; Costa, M.J.; Silva, A.M.; Weinzierl, B.; Esselborn, M.; Petzold, A.; Rasp, K.; Heinold, B.; et al. Properties of dust aerosol particles transported to Portugal from the Sahara Desert. *Tellus B Chem. Phys. Meteorol.* **2009**, *61*, 297–306. [CrossRef]
15. Danylevsky, V.; Ivchenko, V.; Milinevsky, G.; Grytsai, A.; Sosonkin, M.; Goloub, P.; Li, Z.; Dubovik, O. Aerosol layer properties over Kyiv from AERONET/PHOTONS sunphotometer measurements during 2008–2009. *Int. J. Remote Sens.* **2011**, *32*, 657–669. [CrossRef]
16. Milinevsky, G.; Danylevsky, V. Atmospheric Aerosol Over Ukraine Region: Current Status of Knowledge and Research Efforts. *Front. Environ. Sci.* **2018**, *6*, 59. [CrossRef]
17. Amiridis, V.; Balis, D.; Kazadzis, S.; Giannakaki, E.; Papayannis, A.; Zerefos, C. Four years aerosol observations with a Raman lidar at Thessaloniki, Greece, in the framework of European Aerosol Research Lidar Network (EARLINET). *J. Geophys. Res.* **2005**, *110*, D21203. [CrossRef]
18. Papayannis, A.; Mamouri, R.E.; Amiridis, V.; Kazadzis, S.; Perez, C.; Tsaknakis, G.; Kokkalis, P.; Baldasano, J.M. Systematic lidar observations of Saharan dust layers over Athens, Greece in the frame of EARLINET project (2004–2006). *Ann. Geophys.* **2009**, *27*, 3611–3620. [CrossRef]
19. Nisantzi, A.; Mamouri, R.E.; Ansmann, A.; Schuster, G.L.; Hadjimitsis, D.G. Middle East versus Saharan dust extinction-to-backscatter ratios. *Atmos. Chem. Phys.* **2015**, *15*, 7071–7084. [CrossRef]
20. Mamali, D.; Marinou, E.; Sciare, J.; Pikridas, M.; Kokkalis, P.; Kottas, M.; Binietoglou, I.; Tsekeri, A.; Keleshis, C.; Engelmann, R.; et al. Vertical profiles of aerosol mass concentration derived by unmanned airborne in situ and remote sensing instruments during dust events. *Atmos. Meas. Tech.* **2018**, *11*, 2897–2910. [CrossRef]
21. CIMEL. Available online: www.cimel.fr (accessed on 23 September 2022).
22. Holben, B.N.; Eck, T.F.; Slutsker, I.; Tanré, D.; Buis, J.P.; Setzer, A.; Vermote, E.; Reagan, J.A.; Kaufman, Y.J.; Nakajima, T.; et al. AERONET-A Federated Instrument Network and Data Archive for Aerosol Characterization. *Remote Sens. Environ.* **1998**, *66*, 1–16. [CrossRef]
23. Holben, B.N.; Kim, J.; Sano, I.; Mukai, S.; Eck, T.F.; Giles, D.M.; Schafer, J.S.; Sinyuk, A.; Slutsker, I.; Smirnov, A.; et al. An overview of mesoscale aerosol processes, comparisons, and validation studies from DRAGON networks. *Atmos. Chem. Phys.* **2018**, *18*, 655–671. [CrossRef]
24. AERONET (AErosol RObotic NETwork). Available online: http://aeronet.gsfc.nasa.gov/ (accessed on 28 April 2022).
25. Dubovik, O.; King, M.D. A flexible inversion algorithm for retrieval of aerosol optical properties from Sun and sky radiance measurements. *J. Geophys. Res.* **2000**, *105*, 20673–20696. [CrossRef]

26. Dubovik, O.; Holben, B.; Eck, T.F.; Smirnov, A.; Kaufman, Y.J.; King, M.D.; Tanré, D.; Slutsker, I. Variability of absorption and optical properties of key aerosol types observed in worldwide locations. *J. Atmos. Sci.* **2002**, *59*, 590–608. [CrossRef]
27. Dubovik, O.; Sinyuk, A.; Lapyonok, T.; Holben, B.N.; Mishchenko, M.; Yang, P.; Eck, T.F.; Volten, H.; Munoz, O.; Veihelmann, B.; et al. Application of spheroid models to account for aerosol particle nonsphericity in remote sensing of desert dust. *J. Geophys. Res.* **2006**, *111*, D11208. [CrossRef]
28. Holben, B.N.; Tanre, D.; Smirnov, A.; Eck, T.F.; Slutsker, I.; Abuhassan, N.; Newcomb, W.W.; Schafer, J.S.; Chatenet, B.; Lavenu, F.; et al. An emerging ground-based aerosol climatology: Aerosol optical depth from AERONET. *J. Geophys. Res. Atmos.* **2001**, *106*, 12067–12097. [CrossRef]
29. Giles, D.M.; Sinyuk, A.; Sorokin, M.G.; Schafer, J.S.; Smirnov, A.; Slutsker, I.; Eck, T.F.; Holben, B.N.; Lewis, J.R.; Campbell, J.R.; et al. Advancements in the Aerosol Robotic Network (AERONET) Version 3 database-automated near-real-time quality control algorithm with improved cloud screening for Sun photometer aerosol optical depth (AOD) measurements. *Atmos. Meas. Tech.* **2019**, *12*, 169–209. [CrossRef]
30. Sinyuk, A.; Holben, B.N.; Eck, T.F.; Giles, D.M.; Slutsker, I.; Korkin, S.; Schafer, J.S.; Smirnov, A.; Sorokin, M.; Lyapustin, A. The AERONET Version 3 aerosol retrieval algorithm, associated uncertainties and comparisons to Version 2. *Atmos. Meas. Tech.* **2020**, *13*, 3375–3411. [CrossRef]
31. The Cyprus Atmospheric Observatory station in Nicosia, Cyprus Institute at the Athalassa Campus, in Aglantzia. Available online: https://cao.cyi.ac.cy/nicosia/ (accessed on 10 October 2022).
32. The National Ocean Service. Available online: https://oceanservice.noaa.gov/facts/lidar.htm (accessed on 22 April 2022).
33. Popovici, I.E.; Goloub, P.; Podvin, T.; Blarel, L.; Loisil, R.; Unga, F.; Mortier, A.; Deroo, C.; Victori, S.; Ducos, F.; et al. Description and applications of a mobile system performing on-road aerosol remote sensing and in situ measurements. *Atmos. Meas. Tech.* **2018**, *11*, 4671–4691. [CrossRef]
34. Draxler, R.R.; Hess, G.D. An overview of the HYSPLIT 4 modeling system for trajectories, dispersion, and deposition. *Aust. Meteorol. Mag.* **1997**, *47*, 295–308.
35. Stein, A.F.; Draxler, R.R.; Rolph, G.D.; Stunder, B.J.B.; Cohen, M.D.; Ngan, F. NOAA's HYSPLIT atmospheric transport and dispersion modeling system. *Bull. Am. Meteorol. Soc.* **2015**, *96*, 2059–2077. [CrossRef]
36. Global Data Assimilation System (GDAS). National Oceanic and Atmospheric Administration. Available online: https://data.noaa.gov/dataset/dataset/global-data-assimilation-system-gdas (accessed on 13 February 2022).
37. Maring, H.; Savoie, D.L.; Izaguirre, M.A.; Custals, L.; Reid, J.S. Mineral dust aerosol size distribution change during atmospheric transport. *J. Geophys. Res. Atmos.* **2003**, *108*, 8592. [CrossRef]
38. Zhang, Y.; Li, Z.; Zhang, Y.; Li, D.; Qie, L.; Che, H.; Xu, H. Estimation of aerosol complex refractive indices for both fine and coarse modes simultaneously based on AERONET remote sensing products. *Atmos. Meas. Tech.* **2017**, *10*, 3203–3213. [CrossRef]
39. Di Biagio, C.; Formenti, P.; Balkanski, Y.; Caponi, L.; Cazaunau, M.; Pangui, E.; Journet, E.; Nowak, S.; Andreae, M.O.; Kandler, K.; et al. Complex refractive indices and single-scattering albedo of global dust aerosols in the shortwave spectrum and relationship to size and iron content. *Atmos. Chem. Phys.* **2019**, *19*, 15503–15531. [CrossRef]
40. Omar, A.H.; Won, J.-G.; Winker, D.M.; Yoon, S.-C.; Dubovik, O.; McCormick, M.P. Development of global aerosol models using cluster analysis of Aerosol Robotic Network (AERONET) measurements. *J. Geophys. Res.* **2005**, *110*, D10S14. [CrossRef]
41. Szkop, A.; Pietruczuk, A.; Posyniak, M. Classification of aerosol over Central Europe by cluster analysis of aerosol columnar optical properties and backward trajectory statistics. *Acta Geophys.* **2016**, *64*, 2650–2676. [CrossRef]
42. Liu, S.; Liang, X.-Z. Observed diurnal cycle climatology of planetary boundary layer height Shuyan. *J. Clim.* **2010**, *23*, 5790–5809. [CrossRef]
43. Palm, S.P.; Selmer, P.; Yorks, J.; Nicholls, S.; Nowottnick, E. Planetary Boundary Layer Height Estimates From ICESat-2 and CATS Backscatter Measurements. *Front. Remote Sens.* **2021**, *2*, 716951. [CrossRef]
44. Papanikolaou, C.-A.; Papayannis, A.; Mylonaki, M.; Foskinis, R.; Kokkalis, P.; Liakakou, E.; Stavroulas, I.; Soupiona, O.; Hatzianastassiou, N.; Gavrouzou, M.; et al. Vertical Profiling of Fresh Biomass Burning Aerosol Optical Properties over the Greek Urban City of Ioannina, during the PANACEA Winter Campaign. *Atmosphere* **2022**, *13*, 94. [CrossRef]
45. Mona, L.; Amodeo, A.; D'Amico, G.; Giunta, A.; Madonna, F.; Pappalardo, G. Multi-wavelength Raman lidar observations of the Eyjafjallajökull volcanic cloud over Potenza, southern Italy. *Atmos. Chem. Phys.* **2012**, *12*, 2229–2244. [CrossRef]
46. Leon, J.-F.; Derimian, Y.; Chiapello, I.; Tanre, D.; Podvin, T.; Chatenet, B.; Diallo, A.; Deroo, C. Aerosol vertical distribution and optical properties over M'Bour (16.96°W; 14.39°N), Senegal from 2006 to 2008. *Atmos. Chem. Phys.* **2009**, *9*, 9249–9261. [CrossRef]
47. Klett, J.D. Stable analytical inversion solution for processing lidar returns. *Appl. Opt.* **1981**, *20*, 211–220. [CrossRef]
48. Fernald, F.G. Analysis of atmospheric LIDAR observations: Some comments. *Appl. Opt.* **1984**, *23*, 652–653. [CrossRef] [PubMed]
49. Mortier, A.; Goloub, P.; Podvin, T.; Deroo, C.; Chaikovsky, A.; Ajtai, N.; Blarel, L.; Tanre, D.; Derimian, Y. Detection and characterization of volcanic ash plumes over Lille during the Eyjafjallajökull éruption. *Atmos. Chem. Phys.* **2013**, *13*, 3705–3720. [CrossRef]
50. Mortier, A. Tendances et Variabilites de l'aerosol Atmospherique a l'aide du Couplage Lidar. Photometre sur les Sites de Lille et Dakar. Ph.D. Thesis, University of Lille, Lille, France, 2013.
51. Linke, C.; Möhler, O.; Veres, A.; Mohácsi, Á.; Bozóki, Z.; Szabó, G.; Schnaiter, M. Optical properties and mineralogical composition of different Saharan mineral dust samples: A laboratory study. *Atmos. Chem. Phys.* **2006**, *6*, 3315–3323. [CrossRef]

52. Kandler, K.; Lieke, K.; Benker, N.; Emmel, C.; Küpper, M.; Müller-Ebert, D.; Ebert, M.; Scheuvens, D.; Schladitz, A.; Schütz, L.; et al. Electron microscopy of particles collected at Praia, Cape Verde, during the Saharan Mineral Dust Experiment: Particle chemistry, shape, mixing state and complex refractive index. *Tellus Ser. B Chem. Phys. Meteorol.* **2011**, *63*, 475–496. [CrossRef]
53. EOSDIS NASA Worldview. Available online: https://worldview.earthdata.nasa.gov/ (accessed on 10 October 2022).
54. Gong, X.; Wex, H.; Müller, T.; Wiedensohler, A.; Höhler, K.; Kandler, K.; Ma, N.; Dietel, B.; Schiebel, T.; Möhler, O.; et al. Characterization of aerosol properties at Cyprus, focusing on cloud condensation nuclei and ice-nucleating particles. *Atmos. Chem. Phys.* **2019**, *19*, 10883–10900. [CrossRef]
55. Calmer, R.; Roberts, G.C.; Sanchez, K.J.; Sciare, J.; Sellegri, K.; Picard, D.; Vrekoussis, M.; Pikridas, M. Aerosol–cloud closure study on cloud optical properties using remotely piloted aircraft measurements during a BACCHUS field campaign in Cyprus. *Atmos. Chem. Phys.* **2019**, *19*, 13989–14007. [CrossRef]
56. Retalis, A.; Hadjimitsis, D.G.; Michaelides, S.; Tymvios, F.; Chrysoulakis, N.; Clayton, C.R.I.; Themistocleous, K. Comparison of aerosol optical thickness with in situ visibility data over Cyprus. *Nat. Hazards Earth Syst. Sci.* **2010**, *10*, 421–428. [CrossRef]